Revision 1

Precise determination of the effect of temperature on the density of solid and liquid iron, nickel, and tin

Asaka Kamiya, Hidenori Terasaki[*1], Tadashi Kondo

Department of Earth and Space Science, Osaka University

[1]Now at Department of Earth Sciences, Okayama University

[*]Corresponding author: tera@okayama-u.ac.jp

Abstract

Density and thermal expansion coefficient of metals are one of the most fundamental characteristics to describe the equation of state. Especially for liquid metals, the reported data for density and thermal expansion coefficient vary in the literature, even at ambient pressure. To determine density of solid and liquid metals precisely at high temperatures and ambient pressure, we newly developed a high-temperature furnace. The densities of solid Sn, Ni, and Fe were determined from sample image with uncertainty of 0.11%–0.7% in the temperature range of 285–1803 K with increments of 1–10 K. The density of solid Sn decreased linearly with increasing temperature up to 493 K, and the decrease became drastic above that to the melting temperature (T_m). By

contrast, for solid Ni and Fe, the densities decreased linearly with increasing temperature up to the T_m (1728 and 1813 K) without any drastic density drop near T_m. This suggests that Ni and Fe do not exhibit the "premelting effect".

For liquid, the density of liquid Fe was determined with uncertainty of 0.4%–0.7% in the range of 1818–1998 K with temperature increments of 5 K. The obtained thermal expansion coefficient (α) of liquid Fe was well approximated as either a constant value of $\alpha = 2.42(1) \times 10^{-4}$ K^{-1} or a linear function of temperature (T); $\alpha = 1.37(10) \times 10^{-3} - [6.0(6) \times 10^{-7}]T$ [K^{-1}] up to at least 2000 K.

Keywords: Density, Thermal expansion, Metal, Liquid

INTRODUCTION

Density is one of the most fundamental physical properties for understanding planetary interiors. To estimate the structure and composition of a planetary core, the equation of state (EOS) of Fe alloys is an indispensable information, along with planetary exploration data. The density of Fe alloys at ambient pressure is one of the most fundamental characteristics used to describe the EOS, as well as its elastic properties (bulk modulus, K, its pressure derivative [dK_T/dP], and the thermal expansion

coefficient, α). Although the density and thermal expansion of the core constituting metals (Fe and Ni) have been reported, they have not been determined precisely near the melting temperature (T_m). An unusual drastic decrease in the elastic wave velocities near T_m, the so-called "premelting effect," has been reported for some solid metals (Sn and Fe) based both on experiments and theoretical calculations. It is reported to occur at $T/T_m > 0.99$ for Sn at ambient pressure (Nadal and Le Poac, 2003) and at $T/T_m > 0.96$ for Fe at 360 GPa (Martorell et al., 2013a). If the premelting effect occurs in the elastic wave velocity, it could also occur in density, which is closely related to the elastic wave velocity, and thermal expansion. This could significantly influence the EOS and elastic properties of the core. However, the density behaviors of Sn and Fe near T_m have not been precisely known.

For liquid density, the density (ρ) of liquid Fe at ambient pressure has been reported by many authors (e.g., Luca, 1960; 1972; Kirshenbaum and Cahil, 1962; Frohberg and Weber, 1964; Brillo and Egry, 2004; Assael et al., 2006; Kobatake and Brillo, 2013; Le Maux et al., 2019). However, the reported ρ values have some significant deviation ($\Delta\rho$~0.2 g/cm^3 ~2.8%) and the thermal expansion coefficient has not been precisely constrained yet.

In this study, density measurements of solid Sn, Ni, Fe, and liquid Fe were

performed using a newly developed high-temperature furnace with observation windows. The effect of temperature on the density of solid Sn, Ni, Fe, and liquid Fe was precisely investigated at ambient pressure.

METHODS

Experimental methods

The samples were metal rods of Sn (99.9% in purity, Nilaco Corp.), Ni (99.5% in purity, Nilaco Corp.), and Fe (99.9% in purity, Nilaco Corp.). The diameter and height of the sample were 2.99–3.00 and 2.09–3.00 mm, respectively. The top and bottom interfaces of the samples were mirror-polished.

The experiments were conducted using a high-temperature gas furnace (Nagano Co Ltd., Tokyo) installed at Osaka University (Fig. 1a). Heating was performed using a composite resistance heater composed of carbon fiber-reinforced carbon composite (C/C). The C/C heater is superior to generate high temperatures (~2173 K) stably under vacuum or inert gas conditions, and has a small thermal expansion coefficient, which enables rapid heating (~1500 K/min). The C/C heater plate is located around the sample stage and has a slit for sample observation. The sample is set on a sintered alumina plate located at the center of the chamber (Fig.

1b). During the experiment, the temperature was monitored using a K-type thermocouple (TC). The TC junction was located at same height as the sample and 18.6 mm away from the sample center horizontally. The T_m values of Ni and Fe were determined to be 1728 and 1812 K (TC temperature), respectively, based on the shape change of the sample. These results are in good agreement with the literature. Therefore, the temperature at the TC junction was identical to that at the sample center. Temperature was controlled using a proportional integral differential controller. The heating rates were in the range of 3–25 K/min. The measurement was performed under an argon atmosphere at 0.05 MPa (flow rate: 0.8–1.0 l/min).

The chamber had two optical windows for observation of the sample in the horizontal direction. For the density measurements, a charge-coupled device (CCD) (1296(H)x966(V), 12 bit, acA1300–30um; Basler AG) or complementary metal-oxide semiconductor (CMOS) camera (2048(H)x1536(V), 12 bit, BU302MG; Toshiba Teli corp.) was set on one side for optical observation, and a backlight (Fiber optic illuminator) was set on the other (Fig. 1a). The image magnification was optimized using a telecentric zoom lens (x0.5–1.3) (VS Technology Corp.). The pixel size of the image was 3.9–4.5 μm/pixel depending on the magnification. Details of the pixel calibration and evaluation of image distortion are given in Supplement[1] (I). The

exposure time of each image was in the range of 1–80 ms. Images of the sample were taken with 1–10 K steps and analyzed using the method described in next section.

Analytical methods

The density of the sample was obtained from the sample volume at each temperature and initial mass. The sample volume was measured from the 2-dimensional (2D) sample image assuming rotational (cylindrical) symmetry. Image analysis was carried out using ImageJ software (https://imagej.nih.gov/ij/). The sample image was binarized, and brightness profiles of the image were obtained to identify the boundary between the sample and surrounding part.

For solid samples, the diameter and height were measured from the sample brightness profiles (Figs. 2a and 2b). To obtain a clear image of sample bottom boundary which is required for precise determination of the sample height, a small alumina disk is placed underneath the sample (Fig. 2a). In the run AK12 that the small alumina disk was not used, height error of AK12 is much (one-order) larger than that of other runs in which the small disk was used (Supplemental[1] Table S4). The validity of the cylindrical symmetry of the sample was evaluated from images observed from different directions in separate measurements. The sample was put on the rotation stage

109 at room temperature and the image was observed at rotation angles of 0°, 45°, and 90°.
110 For 0–90° rotation, the variations were (1.0–2.0)x10^{-4} cm in diameter and (1.0–3.0)x10^{-4}
111 cm in height, which corresponds to a volume variation of ΔV=(1.4–4.6)x10^{-5} cm³ and a
112 density variation of $\Delta\rho$=(8.4–20.5)x10^{-3} g/cm³ (0.11~0.28%). Therefore, these density
113 variations derived from rotation were small, and the cylindrical symmetry used in this
114 study could be valid for obtaining the sample volume. We included this density
115 variation in the density error (density errors are discussed in next paragraph). The
116 obtained volumes and calculated densities of solid metals (Sn, Ni, and Fe) are
117 summarized in Supplemental[1] Table S1–S3. In some runs, the density of solid sample
118 was measured at room temperature from sample image (see Table S1–S3). The
119 measured density (Sn: 7.278(15), 7.289(13) g/cm^3, Fe: 7.868(9) g/cm^3) agree well with
120 the density database at room temperature (Sn: 7.265 g/cm^3, Fe: 7.874 g/cm^3,
121 Chronological Scientific Tables, 2020). Therefore, it is confirmed that the density
122 obtained from measurement used in this study is consistent with the value of density
123 database.

124 Density error of solid samples contains following contributions. (1) *Errors of*
125 *sample lengths*. The sample diameter and height were obtained from horizontal and
126 vertical brightness profiles of the sample image, respectively (Fig. 2b). The length

127 errors were taken from difference between maximum (minimum) and average measured
128 lengths. The volume (density) error was derived from the propagation of these length
129 errors. The density error derived from length errors are summarized in Supplemental[1]
130 Table S4. (2) *Rotation error*. The sample volume variation derived from sample rotation
131 of 0–90^{o}, as stated in previous paragraph, was included in volume (density) error as
132 summarized in Table S4. (3) *Error of pixel calibration*. As mentioned in supplement (I),
133 length error derived from pixel calibration are 0.004–0.01 μm. The density error derived
134 from this length error is calculated to $3x10^{-4}$–$8x10^{-4}$% based on error propagation,
135 suggesting that the density error from pixel calibration error is negligibly small. Thus,
136 the density error of solid sample in this study correspond to a sum of contribution of
137 length errors and that of rotation error. All these errors are summarized in Table S4. In
138 run AK19, for example, total density errors are 0.137–0.162%, which is obtained from a
139 sum of density error from length errors (0.004–0.027%) and that from rotation error
140 (0.132–0.135%).

141 For liquid samples, the volume of a sample droplet was obtained from a 2D
142 image using Pappus's centroid theorem, which describes the volume of rotating bodies
143 as:

$$V = 2\pi RS \quad (1)$$

where S and R indicate a half area of the sample cross section divided by the rotating axis and the distance between the rotation axis and center of gravity, respectively. The value of S was determined from the 2D image, as shown by the shaded area in Fig. 3a. The sample boundary was identified from the vertical scan of horizontal brightness profiles. The initial image was cut at the rotation axis. Next, the image was binarized, and the area (S) and coordinates of the center of gravity were obtained. More detailed analysis procedure of liquid sample is provided in Supplement[1] (II). The obtained V and ρ of liquid Fe are summarized in Supplemental[1] Table S5. The error in volume was derived from the following errors: (1) error in sample length and rotational symmetry, and (2) error in boundary threshold. (1) We calculated the sample volume using the images of the left and of right halves with equation (1) to verify the assumption of rotational symmetry. The volume (density) difference from left and right half images corresponds to density error derived from rotation. Sample length errors are included in the calculated volume. The results are listed in Supplemental[1] Table S6. In run AK20, for example, the density error from rotation is 0.01–0.038%. This small rotation error indicates that the liquid sample was symmetric to the rotation axis. (2) The error in the boundary threshold is derived mainly from gray pixels (6 to 14 pixels) at the edge boundary of the droplet as shown in the inset of Fig. 3b. We estimated the volume error

by changing the threshold value in the range of the gray pixels. The error in boundary threshold was improved by taking a shadow picture of the sample using a backlight following the method of Le Maux et al. (2019). The backlight has been used in previous studies (e.g., Brillo and Egry 2003; Langstaff et al. 2013; Le Maux et al. 2019). The estimated density error from boundary threshold are listed in Table S6. Thus, the density errors of liquid sample correspond to a sum of these errors (i.e., length, rotation symmetry, and boundary threshold) and summarized in Table S6. For example, in AK20, total density errors are 0.400–0.670%, which is obtained from a sum of density error from rotation and length errors (0.001–0.038%) and that from boundary threshold error (0.027–0.666%).

The recovered samples were mounted in epoxy and polished for textural observation and chemical analysis, which were carried out using a scanning electron microscope (JSM-6010LA; JEOL) equipped with an energy-dispersive spectrometer (NORAN NSS EDX; Thermo Fischer Scientific) with an accelerating voltage of 20 kV. Chemical composition of starting and recovered samples are listed in Supplemental[1] Table S7. Supplemental[1] Fig. S3 shows example of backscattered electron image of the Fe samples quenched from liquid (AK20). From the sample textures of backscattered electron images and chemical composition of the recovered samples, no contamination

was found in the recovered Sn, Ni, and Fe samples (Supplemental[1] Table S7).

RESULTS AND DISCUSSION

Density of tin

The measured density of Sn (body-centered tetragonal [bct] structure) is plotted as a function of temperature in Fig. 4 (Data is found in Supplemental[1] Table S1). The density values from two measurements (AK11 and AK14) were reproducible. The density decreased almost linearly with increasing temperature up to 493 K, which corresponds to $T/T_m < 0.98$. This trend is consistent with a previous study (Touloukian et al., 1975). However, above 493 K, a drastic decrease in density was observed (see Fig. 4). The decrease in density was approximately 0.7%, which is much larger than the density error (0.18–0.22%). This phenomenon was possibly derived from the premelting effect. In a previous study, the premelting effect observed in V_P and V_s at $T/T_m > 0.99$ was considered to occur as a result of decrease in shear modulus (Nadal and Le Poac, 2003). It was found that Sn has a premelting effect near the T_m for both the density and elastic wave velocities.

The thermal expansion coefficient (α) was determined by fitting the density data up to 493 K with equation (2):

198 $$\rho = \frac{\rho_0}{\exp(\int_{T_0}^{T} \alpha dT)} \quad (2),$$

199 where ρ_0 denotes the density at the reference temperature T_0. The α of this study and a
200 previous study are listed in Table 1. In this study, ρ_0 was 7.278(15) at T_0 = 300 K, and
201 the obtained α in the temperature range of 285–490 K was $6.22(3)\times10^{-5}$ K^{-1}. This result
202 was slightly smaller than that in a previous study (6.438×10^{-5} K^{-1}; Touloukian et al.
203 1975).

204

205 **Density of nickel**

206 The measured density of Ni is plotted as a function of temperature in Fig. 5
207 (Data is found in Supplemental[1] Table S2). The densities of two measurements (AK12
208 and AK13) are reproducible. Previous results of Ni density are also plotted in Fig. 5.
209 The density in this study was consistent with that of previous studies (Kohlhaas et al.,
210 1967; Suh et al., 1988; Abdullaev et al., 2015) with an uncertainty of 0.2–0.5%, except
211 for a result of Newkirk et al. (1958). All of these results indicate that there is no drastic
212 decrease in density near T_m, suggesting that face-centered cubic (fcc) Ni does not have
213 the premelting effect on density. This result is different from the density behavior of bct
214 Sn.

215 The density decreases linearly with increasing temperature up to the T_m (1728

K). The α in this study was determined using eq. (2) to 6.18(6)x10^{-5} K^{-1} in the temperature range of 1083–1713 K. The α of the present and previous studies are listed in Table 1. The result of this study is consistent with the previous result (α = 6.07(8)x10^{-5} K^{-1}; Suh et al., 1988) within the error.

Density of solid iron

Densities of solid Fe are plotted as a function of temperature in Fig. 6a together with the result of liquid Fe. The present data is found in Supplemental[1] Table S3. The reproducibility of the measured density was confirmed from four measurements (AK15, AK16, AK18, and AK19) (see Fig. 6a). The two discontinuous density jumps observed at 1162(1) and 1666.0(5) K were derived from phase transitions of the α phase (body-centered cubic (bcc))/γ phase (fcc) and γ phase (fcc)/δ phase (bcc), respectively. Previously reported densities of solid Fe are also plotted in Fig. 6a. Our results are in good agreement with previous studies of α and γ phases (α phase: Straumanis and Kim, 1969; Kohlhaas et al., 1967; γ phase: Onink et al., 1993; Basinski et al., 1955; Kohlhaas et al., 1967) within the error. In the stability field of the δ-phase (1668–1803 K), the density decreases almost linearly with increasing temperature up to near T_m (1813 K) (see Fig. 6b). Thus, the density of solid Fe does not show a drastic decrease near T_m, i.e.,

the premelting effect. This suggests that Fe (bcc) shows a similar behavior with Ni (fcc), while it differs from the behavior of Sn (bct).

The thermal expansion coefficient (α) was determined in each phase of Fe by fitting with equation (2) (Table 1). The α of the α-phase was 4.49(3) $x10^{-5}$ K^{-1} in the range of 823–1163 K, which is consistent with previous result of 4.54(2) $x10^{-5}$ K^{-1} (Straumanis and Kim, 1969). The α of the γ-phase was 6.37(5) $x10^{-5}$ K^{-1} in the range of 1173–1673 K, which is consistent with α = 6.40 $x10^{-5}$ K^{-1} (Komabayashi and Fei, 2010). The α of the δ-phase was 7.02(9) $x10^{-5}$ K^{-1} in the range of 1675–1793 K, which is 35% larger than the result of Kohlhaas et al. (1967) (5.20(21) $x10^{-5}$ K^{-1}). Because the stability field of the δ-phase is a narrow temperature region at high temperature, the number of measured data points in previous studies was limited. By contrast, results of this study supplied more data points and a precise temperature dependence of the density because it was measured with much smaller temperature increments (1–10 K) (Fig. 6b).

Density of liquid iron

The density of liquid Fe is plotted as a function of temperature in Fig. 7 together with the results of previous studies. The data of this study is found in Supplemental[1] Table S5. The reproducibility of the measured density was confirmed

252 from two measurements (AK18 and AK20). The present results are in good agreement
253 with the results of Kirshenbaum and Cahill (1962), Lucas (1960), Brillo and Egry
254 (2004), and Le Maux et al. (2019) within the error. Compared with the previous results,
255 the present results give the density with a smaller error and were measured in the
256 smallest temperature increments of 5 K (Fig. 7).

257 As shown in Fig. 7, the temperature dependence of the density of liquid Fe
258 shows a concave shape. Thus, the α can be well approximated as a linear function of
259 temperature (T); $\alpha = 1.37(10) \times 10^{-3} - (6.0(6) \times 10^{-7})T$ [K^{-1}]. If the α is assumed to be a
260 constant, the average α of AK18 and AK20 is $2.42(1) \times 10^{-4}$ K^{-1}. The α of the present
261 and previous studies are listed in Table 1. The temperature dependence of the α of liquid
262 metals was reported in previous studies (e.g., Kumai and Dass, 1993). The linear
263 temperature dependence of α shows a better fit to the measured density variation
264 (coefficient of determination, R^2, is 0.996) than does the constant value of α (R^2 is
265 0.988). The regression equation of α as a function of temperature is valid, at least, in the
266 temperature range of this study (1818–1998 K).

267

268 # IMPLICATIONS

269 The amount of light elements in the Earth's outer core has been estimated

based on a comparison between the density of the outer core from the seismic model and the EOS of liquid Fe alloys. A constant value of the α of liquid Fe has been widely used in the EOS. However, in this study, the linear temperature dependence of α could be more appropriate for the density variation of liquid Fe. The temperature dependence of α is an important issue to describe the EOS of liquid Fe, and it also needs to be studied at high pressures.

In terms of the premelting effect, it is reported that the premelting effect is connected with rapid increase of defectively coordinated atoms or lattice defects based on numerical calculations (Delogu, 2006a; 2006b; Manai and Delogu, 2007; Martorell et al. 2013a). To evaluate the deviation from solid density, $\rho/\rho_{solid}(T)$ is plotted as a function of temperature in Supplemental[1] Fig. S4, where ρ and $\rho_{solid}(T)$ are measured density and solid density, respectively. The extrapolated value from the linear trend before the premelting is used for the value for $\rho_{solid}(T)$. The $\rho/\rho_{solid}(T)$ decreases suddenly at 485–493 K before melting temperature of 505 K. This may indicate that the fraction of defect (melt) in solid Sn increases by the premelting effect. Alternate expression of melt fraction in solid Sn is given in Supplement[1] (III). Occurrence of the premelting effect in this study is found to be different depending on crystal structures. This is possibly due that the fraction of defect (melt) is characteristic of lattice geometry

(Delogu, 2006b). Further study is necessary to investigate occurrence of the premelting effect for various crystal structures of Fe-alloys at high pressures.

Acknowledgements

The authors acknowledge to H. Ando (Nagano Co., Ltd.) for his technical supports and production of the furnace and also thank to T. Komabayashi, T. Sakaiya and T. Taniguchi for fruitful discussion. The author would like to thank two anonymous reviewers for insightful comments on earlier version of this manuscript. This work in partly supported by Grants-in-aid for scientific research from the Ministry of Education, Culture, Sport, and Science and Technology (MEXT) (15H05828, 26247089, and 20H02008).

REFERENCES CITED

Abdullaev, R.N., Kozlovskii, Y.M., Khairulin, R.A., and Stankus, S.V. (2015) Density and Thermal Expansion of High Purity Nickel over the Temperature Range from 150 K to 2030 K. International Journal of Thermophysics, 36, 603-619.

Assael, M.J., Kakosimos, K., Banish, R.M., Brillo, J., Egry, I., Brooks, R., Quested, P.N., Mills, K.C., Nagashima, A., Sato, Y., and Wakeham, A.W. (2006) Reference Data for the Density and Viscosity of Liquid Aluminum and Liquid Iron. Journal of

306 Physical and Chemical Reference Data 35, 285.

307 Basinski, Z.S., Hume-Rothery, W., and Sutton, A.L. (1955) The lattice expansion of iron.

308 Proceedings of the Royal Society, Ser. A 229, 459–467.

309 Brillo, J. and Egry I. (2003) Density determination of liquid copper, nickel, and their

310 alloys. International Journal of Thermophysics, 24, 1155–1170.

311 Brillo, J. and Egry I. (2004) Density and excess volume of liquid copper, nickel, iron,

312 and their binary alloys. Zeitschrift für Metallkunde, 95, 691.

313 Chronological Scientific Tables, National Astronomical Observatory of Japan (Ed),

314 (2020) Maruzen.

315 Delogu, F. (2006a) Mechanistic aspects of homogeneous and heterogeneous melting

316 processes. Journal of Physical Chemistry, 110, 12645–12652.

317 Delogu, F. (2006b) Homogeneous melting of metals with different crystalline structure.

318 Journal of Physics: Condensed Matter, 18, 5639–5653.

319 Frohberg, M.G. and Weber, R. (1964) Archiv für das Eisenhüttenwesen, 35, 877.

320 Kobatake, H., and Brillo, J. (2013) Density and viscosity of ternary Cr–Fe–Ni liquid

321 alloys. Journal of Materials Science, 48, 6818–6824.

322 Kohlhaas, R., Dunner, P., and Schmitz-Pranghe N. (1967) The temperature-dependence

323 of the lattice parameters of iron, cobalt, and nickel in the high temperature range.

Zeitschrift für angewandte Mathematik und Physik, 23, 245.

Komabayashi, T., and Fei, Y. (2010) Internally consistent thermodynamic database for iron to the Earth's core conditions. Journal of Geophysical Research, 115, B03202.

Kirshenbaum, A.D., and Cahill, J.A. (1962) The density of liquid NaCl and KCl and an estimate of their critical constants together with those of the other alkali halides. Transactions of the Metallurgical Society of AIME 224, 816.

Kobatake, H., and Brillo, J. (2013) Density and thermal expansion of Cr–Fe, Fe–Ni, and Cr–Ni binary liquid alloys. Journal of Materials Science volume 48, 4934–4941.

Kumai, M., and Dass, N. (1993) Temperature dependence of density and thermal expansion in some liquid metals. Journal of Non-Crystalline Solids, 156–158, Part 1, 2,417–420.

Langstaff, D., Gunn, M., Greaves, G.N, Marsing, A., and Kargl, F. (2013) Aerodynamic levitator furnace for measuring thermophysical properties of refractory liquids. Review of Scientific Instruments, 84, 124901.

Le Maux, D., Courtois, M., Pierre, T., Lamien, B., and Le Masson, P. (2019) Density measurement of liquid 22MnB5 by aerodynamic levitation. Review of Scientific Instruments, 90, 074904.

Lucas, L.D. (1960) Densite du fer, du nickel et du cobalt a l'etat liquid. Comptes Rendus

342 de l'Academie des Sciences, 250, 1850–1852.

343 Lucas, L.D. (1972) Densite de metaux a haute temperature (dans les etats solide et
344 liquide). Memoires et Etudes Scientifiques de la Revue de Metallurgie, 69, 479–492.

345 Manai, G. and Delogu, F. (2007) Numerical simulations of the melting behavior of bulk
346 and nanometer-sized Cu systems. Physica B, 392, 288–297.

347 Martorell, B., Vočadlo, L., Brodholt, J., and Wood, I.G. (2013a) Strong Premelting
348 Effect in the Elastic Properties of hcp-Fe Under Inner-Core Conditions. Science, 342,
349 466.

350 Martorell, B., Brodholt, J., Wood, I.G., and Vočadlo, L. (2013b) The effect of nickel on
351 the properties of iron at the conditions of Earth's inner core: Ab initio calculations of
352 seismic wave velocities of Fe–Ni alloys. Earth and Planetary Science Letters, 365,
353 143–151.

354 Nadal, M.H., and Le Poac, P. (2003) Continuous model for the shear modulus as a
355 function of pressure and temperature up to the melting point: Analysis and
356 ultrasonic validation. Journal of Applied Physics, 93, 2472–2480.

357 Newkirk Jr., H.W. and Sisler, H.H. (1958) Determination of Residual Stresses in
358 Titanium Carbide - Base Cermets by High - Temperature X - Ray Diffraction.
359 Journal of the American Ceramic Society, 41, 93.

Onink, M., Brakman, C.M., Tichelaar, F.D., Mittemeijer, E.J., Zwaag, S., Root, J.H., and Konyer, N.B. (1993) The lattice parameters of austenite and ferrite in Fe-C alloys as functions of carbon concentration and temperature. Scripta Metallurgica, 29, 1011.

Sola, E., and Alfè, D. (2009) Melting of Iron under Earth's Core Conditions from Diffusion Monte Carlo Free Energy Calculations. Physical Review Letters, 103, 078501–078504.

Straumanis, M.E., and Kim, D.C. (1969) Lattice constants, thermal expansion coefficients, densities, and perfection of structure of pure iron and of iron loaded with hydrogen. Zeitschrift für Metallkunde, 60, 272.

Suh, I.K., Ohta, H., Waseda, Y., and Mater, J. (1988) High-temperature thermal expansion of six metallic elements measured by dilatation method and X-ray diffraction, Science 23, 757.

Touloukian, Y.S., Kirby, R.K., Taylor, R.E., and Desai, P.D. (1975) Thermophysical Properties of Matter, 12, 339 p, Plenum, New York

Endnote:

Deposit item ---, Supplemental Material. Deposit items are free to all readers and found

on the MSA website, via the specific issue's Table of Contents.

Figure captions

Fig. 1 (a) High-temperature furnace and measurement set-up. (b) Heater and sample view from the top inside the chamber. The C/C heater has a slit for sample observation. The sample rod is 3 mm in diameter. Cross denotes the position of thermocouple junction.

Fig. 2 (a) Binarized image of solid Fe at 1473 K (AK16). Small alumina disk was inserted between the sample and large alumina plate. The sample bottom interface without alumina support was kept in flat even high temperatures (Fig. 2a). (b) Horizontal brightness profile of the area shown by dashed square in (a). Sample boundary was determined from the brightness profile. Diameter error corresponds difference between max. and min. diameter values.

Fig. 3 (a) Schematic image of liquid sample droplet for application to Pappus's centroid theorem. Shaded area (S) denotes a half area of the sample cross section divided by the rotating axis (y). R denotes the distance between the rotation axis (y) and center of gravity (G). (b) Raw image of liquid Fe at 1818 K (AK20). (Inset) Gray pixels (1–6 pixels) at the top boundary of the sample.

Fig. 4 The effect of temperature on the density of solid Sn. Open and solid circles

398 respectively denote the results of AK11 and AK14 of this study. The results of
399 two measurements are reproducible. Dashed line represents the trend reported
400 by Touloukian et al. (1975). Vertical dotted lines denote T/T_m=0.98 (493 K)
401 and 1.0 (505 K).

402 Fig. 5 The effect of temperature on the density of solid Ni. Bold dotted and thin
403 dashed lines denote linear fit to the density data of this study and that of
404 Abdullaev et al. (2015), respectively. Vertical dotted line represents the T_m
405 (1728 K). Since small alumina disk was not put beneath the sample in AK12,
406 height error of this run was relatively large, causing the larger density error
407 (see Supplemental[1] Table S4).

408 Fig. 6 (a) The effect of temperature on the density of solid and liquid Fe. Vertical
409 lines at 1162, 1666, and 1813 K denote the phase transitions of α phase
410 (bcc)/γ phase (fcc), γ phase (fcc)/δ phase (bcc), and δ phase (bcc)/liquid,
411 respectively. (b) A zoom-in plot of high temperature part of γ and δ phases
412 (1600–1820 K).

413 Fig. 7 The effect of temperature on the density of liquid Fe. Bold dotted curve
414 represents fit to the density data using a linear temperature dependence of α
415 ($\alpha = 1.37(10) \times 10^{-3} - (6.0(6) \times 10^{-7})T$ [K^{-1}]).

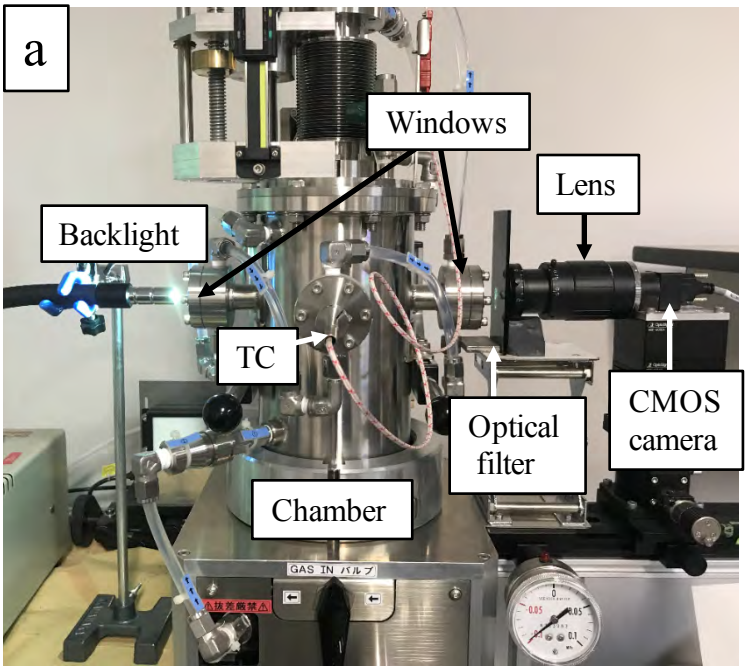
a
Windows
Lens
Backlight
TC
Optical filter
CMOS camera
Chamber
GAS IN バルブ

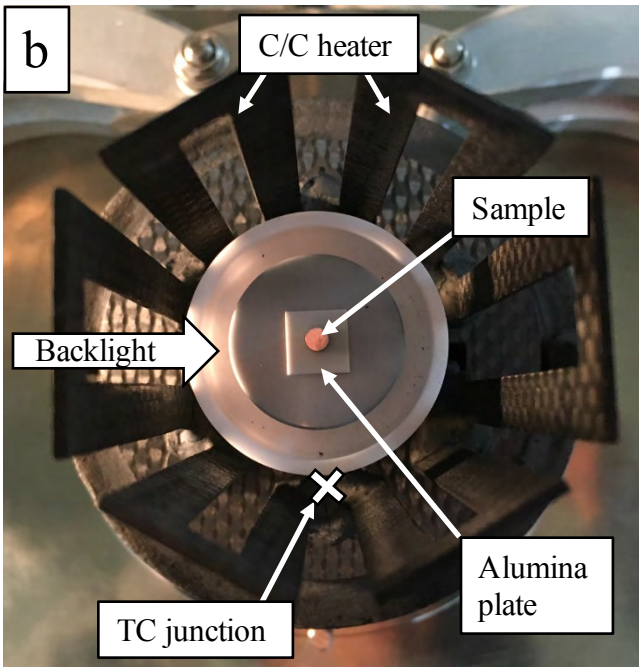
b
C/C heater
Sample
Backlight
Alumina plate
TC junction

Figure 1

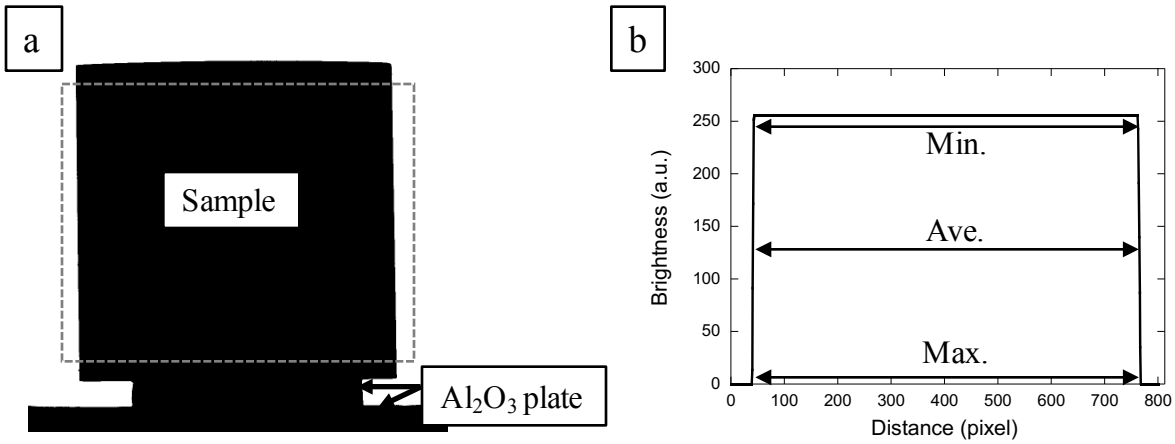
a
Sample
Al_2O_3 plate
b
Brightness (a.u.)
Distance (pixel)
Min.
Ave.
Max.
0
50
100
150
200
250
300
0
100
200
300
400
500
600
700
800

Figure 2

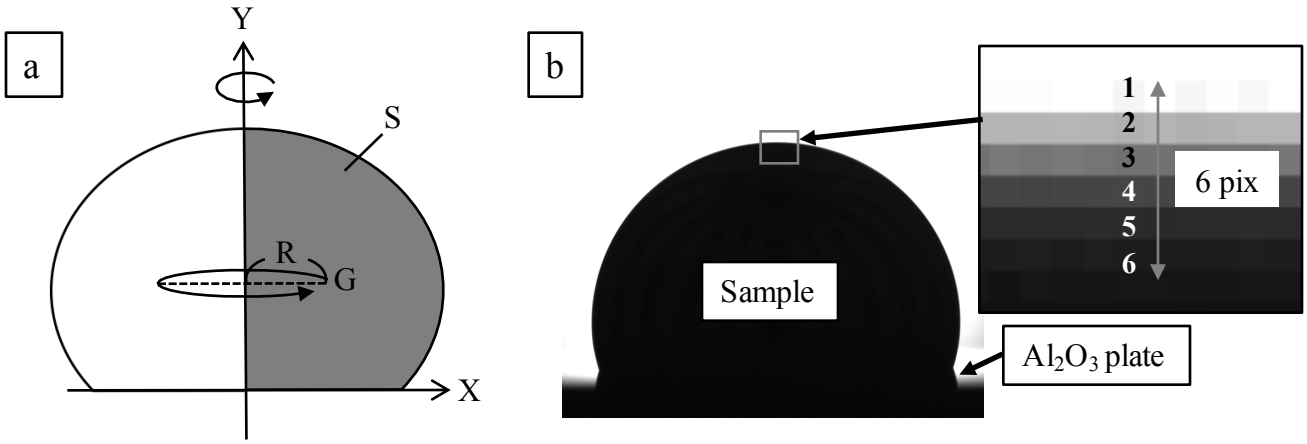

Figure 3

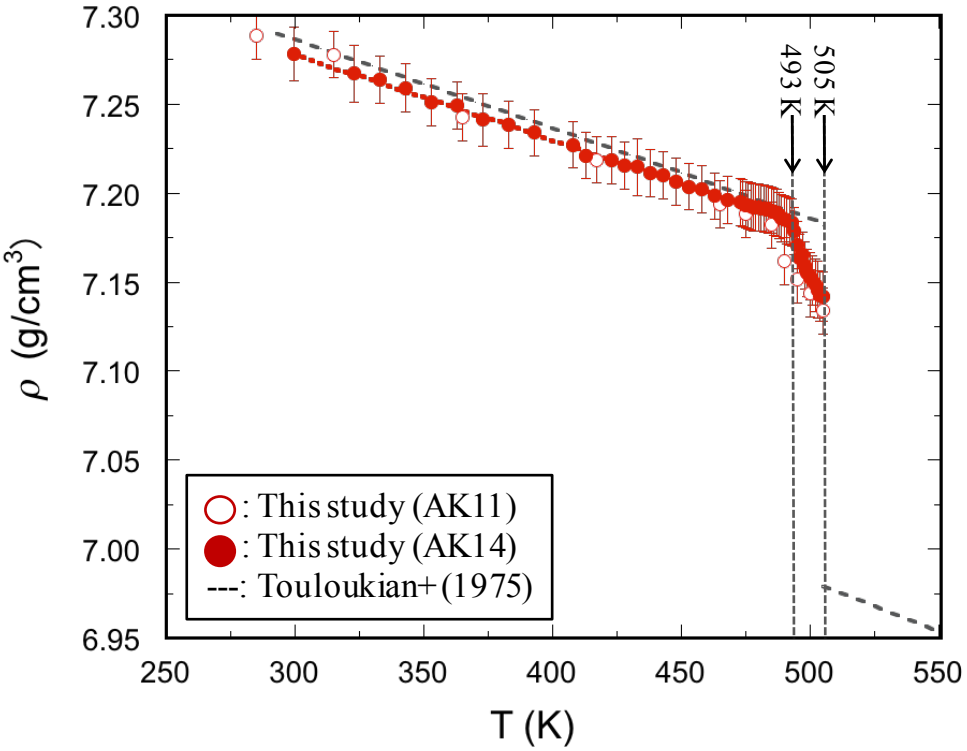
7.30
7.25
7.20
7.15
7.10
7.05
7.00
6.95
ρ (g/cm3)
250
300
350
400
450
500
550
T (K)
493 K
505 K
: This study (AK11)
: This study (AK14)
---: Touloukian+(1975)

Figure 4

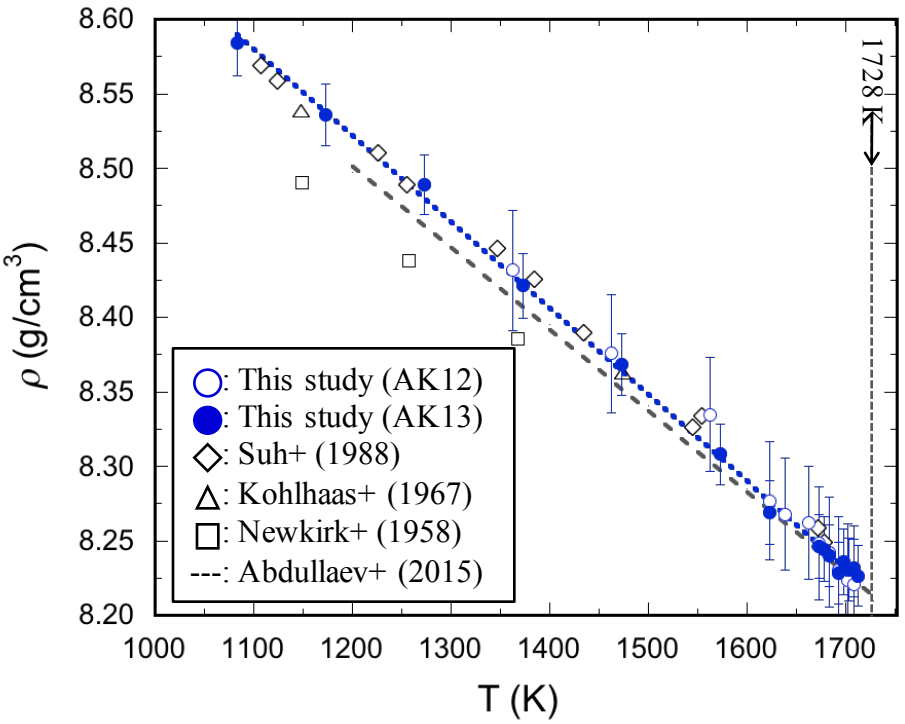
8.60
8.55
8.50
8.45
8.40
8.35
8.30
8.25
8.20
ρ (g/cm3)
1000
1100
1200
1300
1400
1500
1600
1700
T (K)
1728 K
○: This study (AK12)
●: This study (AK13)
◇: Suh+ (1988)
△: Kohlhaas+ (1967)
□: Newkirk+ (1958)
---: Abdullaev+ (2015)

Figure 5

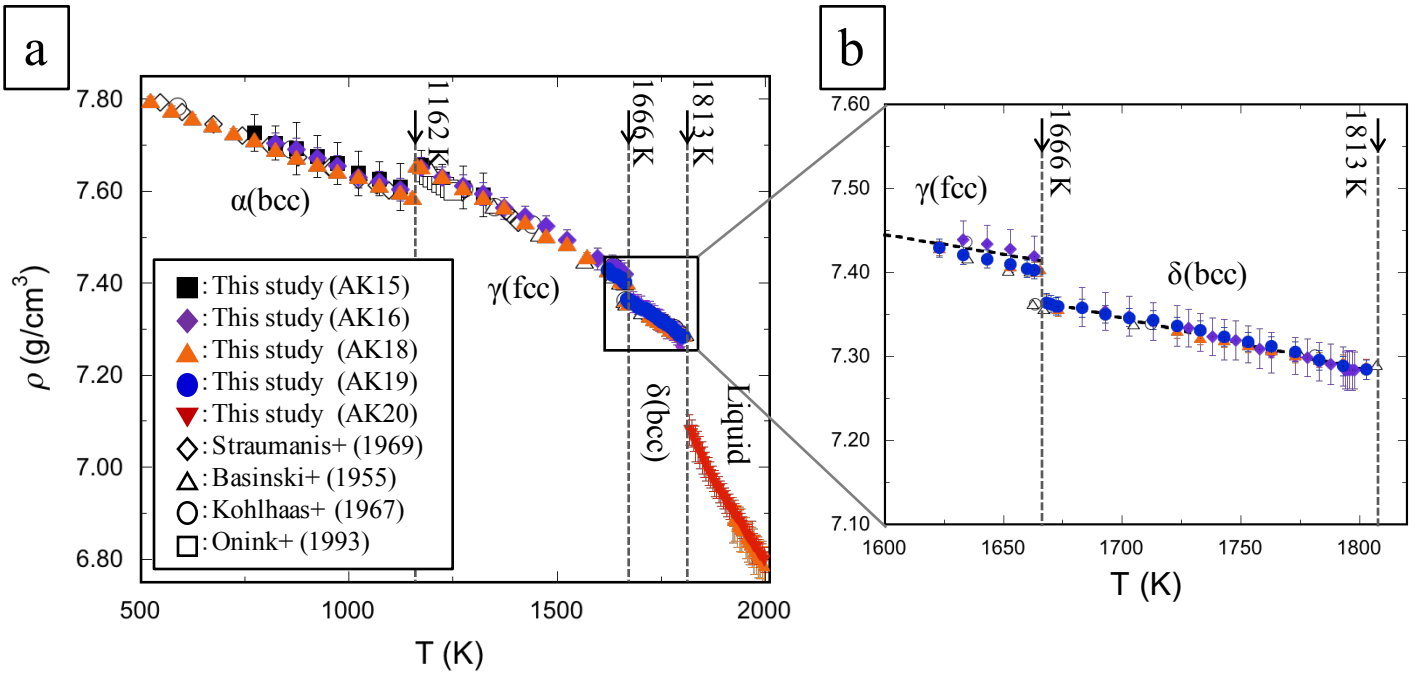
a
b
ρ (g/cm3)
T (K)
1162 K
1666 K
1813 K
α(bcc)
γ(fcc)
δ(bcc)
Liquid
: This study (AK15)
: This study (AK16)
: This study (AK18)
: This study (AK19)
: This study (AK20)
: Straumanis+ (1969)
: Basinski+ (1955)
: Kohlhaas+ (1967)
: Onink+ (1993)

Figure 6

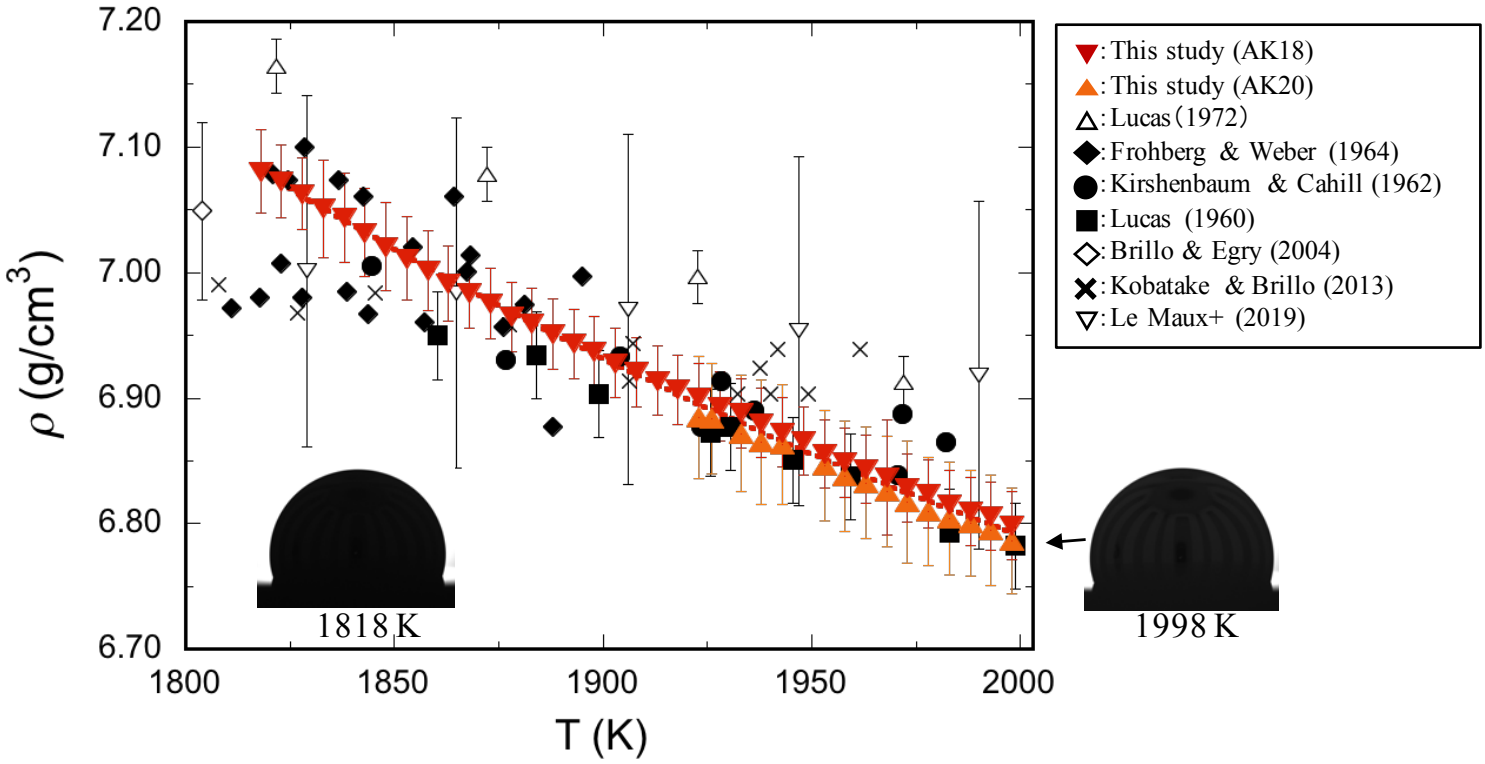
7.20
7.10
7.00
6.90
6.80
6.70
ρ (g/cm3)
1800
1850
1900
1950
2000
T (K)
1818 K
1998 K
▼: This study (AK18)
▲: This study (AK20)
△: Lucas (1972)
◆: Frohberg & Weber (1964)
●: Kirshenbaum & Cahill (1962)
■: Lucas (1960)
◇: Brillo & Egry (2004)
✕: Kobatake & Brillo (2013)
▽: Le Maux+ (2019)

Figure 7

Table 1. Thermal expansion coefficient (α) of solid and liquid metals in this study and previous studies.[*]

Sample	phase	ρ_0 [g/cm³]	T_0 [K]	T range [K]	a^{**} [10^{-5} /K]	b^{**} [10^{-7}/K]	Method	Reference
Sn	bct	7.278	300	285-490	6.22 (3)		Image	This study (AK11,14)
Ni	fcc	8.584	1083	1083-1713	6.18 (6)		Image	This study (AK12,13)
Fe	α-bcc	7.868	295	295-1153	4.49 (3)		Image	This study (AK15-18)
Fe	γ-fcc	7.653	1173	1163-1665.5	6.37 (5)		Image	This study (AK15-18)
Fe	δ-bcc	7.365	1668	1668-1803	7.02 (9)		Image	This study (AK16-19)
Fe	liquid	7.081	1818	1818-1998	24.2 (1)		Image	This study (AK18,20)
Fe	liquid	7.081	1818	1818-1998	137 (10)	-6.0(6)	Image	This study (AK18,20)
Sn	bct	7.290	293		6.44			Touloukian et al. (1975)
Ni	fcc	8.626	976	976-1678	6.07 (8)		X-ray diff.	Suh et al. (1988)
Ni	fcc	8.497	1200	1200-1728	6.40 (6)		Gamma method	Abdullaev et al. (2015)
Fe	α-bcc	7.840	427	427-1023	4.54 (2)		X-ray diff.	Straumanis and Kim (1969)
Fe	γ-fcc	7.533	1400	1400-1600	6.4(1)		X-ray diff.	Komabayashi and Fei (2010)
Fe	δ-bcc	7.362	1663	1663-1781	5.20 (21)		X-ray diff.	Kohlhaas et al. (1967)
Fe	liquid	7.164	1822	1822-1972	23.7 (9)		Archimedean	Lucas (1972)
Fe	liquid	6.95	1860	1860-2477	14.3 (5)		Archimedean	Lucas (1960)
Fe	liquid	7.005	1845	1845-2448	16.0 (2)		Archimedean	Kirshenbaum and Cahill (1962)
Fe	liquid	6.99	1808	1808-1961	7.9 (7)		Image	Kobatake and Brillo (2013)

[*]Numbers in parenthesis indicate an error in last digit(s).

[**]α is expressed using a linear function of T as $\alpha=a+bT$